AD-A108 687 SCIENCE APPLICATIONS INC MCLEAN VA F/G 8/3
A DYNAMICAL MODEL OF WIND-INDUCED NEAR-INERTIAL MOTIONS.(U)
NOV 81 D M RUBENSTEIN N00014-81-C-0084
UNCLASSIFIED SAI-82-598-WA NL

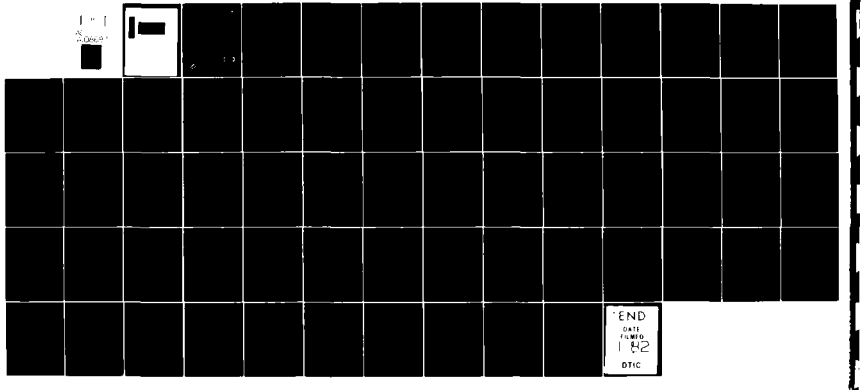

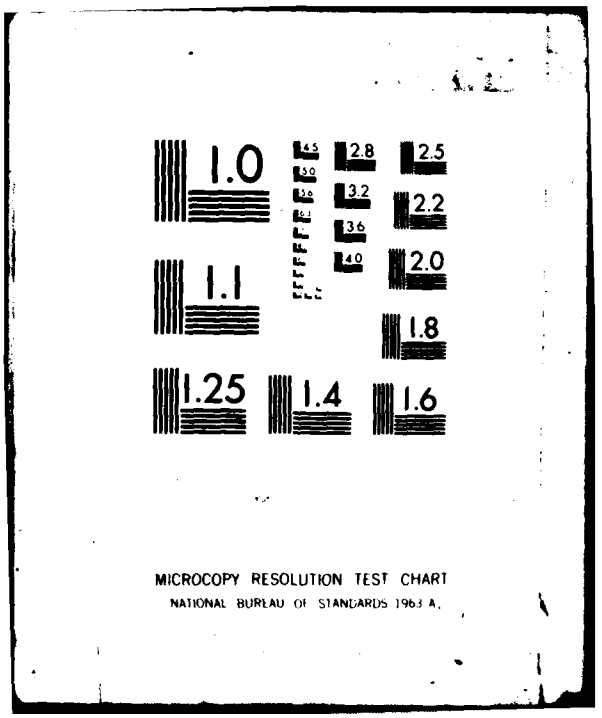
1.0
1.1
1.25
1.4
1.6
1.8
2.0
2.2
2.5
2.8
3.2
3.6
4.0
MICROCOPY RESOLUTION TEST CHART
NATIONAL BUREAU OF STANDARDS 1963 A.

A DYNAMICAL MODEL OF WIND-INDUCED NEAR-INERTIAL MOTIONS

SAI-82-598-WA

SAI

ATLANTA • ANN ARBOR • BOSTON • CHICAGO • CLEVELAND • DENVER • HUNTSVILLE • LA JOLLA
LITTLE ROCK • LOS ANGELES • SAN FRANCISCO • SANTA BARBARA • TUCSON • WASHINGTON

A DYNAMICAL MODEL OF WIND-INDUCED NEAR-INERTIAL MOTIONS

SAI-82-598-WA

OPD-TR-424-81-274-02

November 1981

Prepared by:
David Rubenstein

Prepared for:
Naval Ocean Research and Development Activity
NSTL Station, Mississippi 39529

Prepared Under Contract No.
N00014-81-C-0084

SCIENCE APPLICATIONS, INC.
1710 Goodridge Drive
P.O. Box 1303
McLean, Virginia 22102
(703) 821-4300

UNCLASSIFIED

SECURITY CLASSIFICATION OF THIS PAGE (When Data Entered)

REPORT DOCUMENTATION PAGE	READ INSTRUCTIONS BEFORE COMPLETING FORM
1. REPORT NUMBER: SAI-82-598-WA	2. GOVT ACCESSION NO.: AD-A108 687
	3. RECIPIENT'S CATALOG NUMBER:
4. TITLE (and Subtitle): A Dynamical Model of Wind-Induced Near-Inertial Motions	5. TYPE OF REPORT & PERIOD COVERED: Technical Report 11/80 - 10/81
	6. PERFORMING ORG. REPORT NUMBER: SAI-82-598-WA
7. AUTHOR(s): David M. Rubenstein	8. CONTRACT OR GRANT NUMBER(s): N00014-81-C-0084
9. PERFORMING ORGANIZATION NAME AND ADDRESS: Science Application, Inc. 1710 Goodridge Drive P. O. Box 1303 McLean, VA 22102	10. PROGRAM ELEMENT, PROJECT, TASK AREA & WORK UNIT NUMBERS:
11. CONTROLLING OFFICE NAME AND ADDRESS: NORDA Code 540 Ocean Measurements Program NSTL Station, Bay St. Louis, MS 39529	12. REPORT DATE: November 1981
	13. NUMBER OF PAGES:
14. MONITORING AGENCY NAME & ADDRESS(if different from Controlling Office): same	15. SECURITY CLASS. (of this report): unclassified
	15a. DECLASSIFICATION/DOWNGRADING SCHEDULE:

16. DISTRIBUTION STATEMENT (of this Report)

Approved for public release; distribution unlimited.

17. DISTRIBUTION STATEMENT (of the abstract entered in Block 20, if different from Report)

Approved for public release; distribution unlimited.

18. SUPPLEMENTARY NOTES

19. KEY WORDS (Continue on reverse side if necessary and identify by block number)

Inertial Oscillations
Internal Waves
Shear
Fluid Dynamics
Ekman Layer

20. ABSTRACT (Continue on reverse side if necessary and identify by block number)

A semispectral model of upper ocean inertial motions is developed. The model is solved with a Fourier-Chebyshev expansion in the spatial dimensions, and numerically in time. The model allows the user to specify arbitrary vertical profiles of mean stratification and eddy diffusivity. The model is driven by a wind stress function which is an arbitrary function of time

DD FORM 1 JAN 73 1473 EDITION OF 1 NOV 65 IS OBSOLETE
S/N 0102-LF-014-6601

SECURITY CLASSIFICATION OF THIS PAGE (When Data Entered)

The model is tested against analytic time-dependent Ekman-layer solutions. The comparisons are excellent.

The model is used to simulate the response to a delta-function wind stress impulse. Two cases are presented; one with uniform profiles of stratification and eddy diffusivity, and one with nonuniform profiles. Response functions of wavenumber and frequency are computed for current velocity and shear. The response is shown to be in resonance near the lowest two modes of the internal wave dispersion relation.

TABLE OF CONTENTS

LIST OF FIGURES

Section 1
INTRODUCTION

Inertial oscillations in the upper ocean have been receiving a good deal of attention in recent years. Pollard (1980) showed that much of the kinetic energy measured by stationary current meters is contained in the near-inertial range. From the same data set, Rubenstein and Newman (1981) showed that shear was also predominant in this frequency range.

In this technical report, we present the development of a dynamical model, validations and results. The purpose of this model is to simulate wind forced internal waves in the near inertial frequency band.

The most complete modeling effort of near inertial frequency internal waves is related in a series of papers by Krauss (1976a,b: 1978a,b: 1981). Krauss bases his model on the hydrodynamical equations of motion in a viscous, Boussinesq, rotating fluid. The latter three of these papers consider the generation of internal waves in a flat bottomed channel of finite width and depth, and of infinite length.

In the present work we make some minor changes to Krauss' model equations: We ignore the horizontal eddy diffusivity terms, and we assume the hydrostatic approximation. We choose a coordinate system with z aligned positive upwards, x is aligned across the width of the channel and y is along the length of the channel. Table

1.1 is a list of the variables. For a complete development of the model equations, we refer the reader to Rubenstein (1981). The equations are listed below.

$$\frac{\partial u}{\partial t} - fv = -\frac{\partial p}{\partial x} + \frac{\partial}{\partial z}\left(\nu \frac{\partial u}{\partial z}\right), \tag{1.1}$$

$$\frac{\partial v}{\partial t} + fu = \frac{\partial}{\partial z}\left(\nu \frac{\partial v}{\partial z}\right), \tag{1.2}$$

$$0 = -\frac{\partial p}{\partial z} + b, \tag{1.3}$$

$$\frac{\partial b}{\partial t} + N^2 w = 0, \tag{1.4}$$

$$\frac{\partial u}{\partial x} + \frac{\partial w}{\partial z} = 0 \tag{1.5}$$

Here, we have set to zero all derivatives with respect to y. We have also neglected the buoyancy eddy diffusivity term, and the processes which maintain the mean buoyancy profile against diffusion. The boundary conditions are as follows.

$$w = 0 \quad \text{at } z = 0, D, \tag{1.6}$$

$$\frac{\partial u}{\partial z} = \frac{\partial v}{\partial z} = 0 \text{ at } z = 0, \tag{1.7}$$

$$\nu \left(\frac{\partial u}{\partial z}, \frac{\partial v}{\partial z}\right) = -\underline{\tau}\,(x,t) \text{ at } z = D, \tag{1.8}$$

$$u = 0 \quad \text{at } x = 0, L. \tag{1.9}$$

The surface stress vector $\tau(x,t)$ is a prescribed function which drives the system. Equations (1.6) and (1.9) state that velocities normal to the channel boundary surfaces should vanish. Equation (1.7) prescribes that the stress, and therefore the shear at the bottom

Table 1.1

DEFINITIONS OF VARIABLES

x, y, z	Right-handed coordinate system, z positive up, z = 0 at bottom, D at surface.
u, v, w	Velocity components
t	Time
p	p'/ρ_o, where p' is pressure fluctuation from a reference state, and ρ_o is a representative value of density
ν	Eddy diffusivity, a function of z^* only
N	Vaisala frequency; $N^2 = -\left(\frac{g}{\rho_o}\frac{d\rho_r}{dz}\right)$, where $\rho_r(z)$ is a reference state of density.
b	Buoyancy; $-\rho' g/\rho_o$, where ρ' is density fluctuation from a reference state.
f	Inertial frequency = $2\Omega \sin(\text{latitude})$

should be zero. This boundary condition allows slippage at the bottom, which, after all, is an artifice of the model.

Krauss solves his model equations by expanding his dependent variables into Fourier series in range (x^*) and in time (t^*), and solving the resulting depth dependent equations numerically. In essence, his surface stress functions and solutions are either of the form (1978a)

$$\psi = \sum_{+,-} \sum_{k=1}^{K} \psi_k^{\pm} e^{\mp i\omega t} \sin k\pi x \qquad (1.10)$$

or of the form (1978b)

$$\psi = \sum_{+,-} \sum_{k=1}^{K} \psi_k^{\pm} e^{\mp ik\pi(x - ct)} \qquad (1.11)$$

The form of (1.10) is that of a standing wave, and (1.11) represents a propagating wave. Since the frequency ω in (1.10) and the propagation speed c in (1.11) are constants, both forms are periodic in space and time, and are non-dispersive.

We feel that these constraints are too restrictive. A wind pattern does not necessarily propagate at a constant velocity, in a nondispersive manner. A sudden wind event does not force a current response which is periodic in time--instead the response is generally transient in nature. Therefore we choose to solve the equations of motion without assuming perodicity in time. We expand the horizontal dependences in terms of a truncated Fourier series, and the vertical in terms of a truncated Chebyshev polynomial series. The resulting equations are marched

forward in time using a finite difference scheme, starting from an initial "at rest" condition. We justify our choices as follows.

We do not include horizontal eddy diffusivity terms in our equations. Therefore, there are no frictional boundary layers adjacent to the lateral channel boundaries. There should be no numerical convergence problems in the vicinity of these boundaries, so the use of Fourier series is advantageous. We do include vertical eddy diffusivity, which, in conjunction with the surface stress forcing, leads to a very sharp frictional boundary layer near the surface. Since the convergence of a Fourier series depends critically on the continuity at the boundary endpoints, a Fourier expansion is not well suited for the vertical dimension. On the other hand, Chebyshev series are not affected by the Gibbs overshoot phenomenon, as long as the interior of the domain is continuous (Gottlieb and Orszag, 1977). Their convergence properties make Chebyshev series an ideal choice for expansion in the vertical.

This report is a companion to the paper entitled "Models of Near Inertial Vertical Shear", (Rubenstein and Grabowski, 1981). This previous paper gives much of the theoretical framework upon which the present report is based. We encourage the reader who is not familiar with the theory of near-inertial frequency motions to look at Section 1 of this previous paper, which provides a derivation of the model equations, and Section 3, which discusses internal wave resonances.

The plan for the present report is as follows. In Section 2 the method of solution is explained in detail.

The spectral and finite difference equations used in our numerical model are developed. Section 3 presents a validation of the model. Comparisons between model results and analytically derived solutions are shown. Section 4 develops an analytic solution to the initial start-up problem. The results there give us a handle for understanding some of the numerical results presented in Section 5. In Section 6 we briefly summarize this report and emphasize our conclusions.

Section 2
METHOD OF SOLUTION

2.1 MODEL EQUATIONS

In this section we present the model equations, and develop their method of solution. We begin with the equations (1.1) - (1.8), and nondimensionalize the variables as follows (asterisks denote dimensional variables):

$$
\begin{aligned}
t^* &= tf^{-1} \quad , \\
z^* &= zD \quad , \\
x^* &= xL \quad , \\
u^* &= u(Lf) \quad , \\
v^* &= v(Lf) \quad , \\
w^* &= w(Df) \quad , \\
p^* &= p(L^2f^2) \quad , \\
\mu^* &= \mu(D^2f) \quad , \\
N^* &= n(f/\delta) \quad , \\
b^* &= b(f^2L/\delta) , \\
\underline{\tau}^* &= \underline{\tau}(LDf^2) \quad . \qquad (2.1a\text{-}k)
\end{aligned}
$$

Here, D is the depth and L is the width of the channel. The nondimensional equations and boundary conditions become

$$
\begin{aligned}
\partial_t u - v &= -\partial_x p + \partial_z(\mu \partial_z u) , \\
\partial_t v + u &= \partial_z(\mu \partial_z v) \quad , \\
0 &= -\partial_z p + b \quad , \\
\partial_t b + n^2 w &= 0 \quad , \\
\partial_x u + \partial_z w &= 0 \quad , \qquad (2.2a\text{-}e)
\end{aligned}
$$

$$w = \partial_z u = \partial_z v = 0 \text{ at } z = 0 ,$$

$$w = 0;\ \mu\partial_z u = -\tau^x(x,t),\ \mu\partial_z v = -\tau^y(x,t) \text{ at } z = 1 ,$$

$$u = 0 \text{ at } x = 0,1 . \qquad (2.3a\text{-}c)$$

2.2 FOURIER-CHEBYSHEV EXPANSION

We choose to eliminate variables by combining (2.2a-e) into two equations in v and w:

$$\partial_{zztt} w + \partial_{xzt} v - \partial_{zz}\left(\mu\partial_{zzt} w\right) + n^2\partial_{xx} w = 0. \qquad (2.4)$$

$$\partial_{xt} v - \partial_z w - \partial_z\left(\mu\partial_{xz} v\right) = 0 . \qquad (2.5)$$

Equations (2.4) and (2.5) constitute a parabolic system, sixth order in z, and third order in t.

We look for an approximate truncated Fourier-Chebyshev solution of the form

$$v = \sum_{k=1}^{M} \sum_{j=0}^{N} V_{jk}(t) T_j(z) \sin k\pi x \qquad (2.6)$$

$$w = \sum_{k=1}^{M} \sum_{j=0}^{N} W_{jk}(t) T_j(z) \cos k\pi x . \qquad (2.7)$$

The functions $T_j(z)$ are j-order Chebyshev polynomials, and N is their truncation order. In order to satisfy the lateral boundary conditions (2.3c), v is proportional to $\sin k\pi x$. From the form of (2.5), it follows that w should be proportional to $\cos k\pi x$.

We substitute (2.6), (2.7) into (2.5) to obtain

$$\sum_{j=0}^{N}\left[k\dot{=}V_{jk}\dot{T}_j - (\mu' k\dot{=}V_{jk} + fW_{jk})T_j - \mu k V_{jk}T_j\right] = 0 \tag{2.8}$$

Here the dot indicates a time derivative, and each prime indicates differentiation with respect to z. For simplicity of solution, we require that $\mu(z)$ be an even function, and that it can be written

$$\mu(z) = \sum_{r=0}^{R} a_r z^{2r} , \tag{2.9}$$

where R is less than N. Using the notation developed in Appendix A, we expand (2.9) in terms of Chebyshev polynomials.

$$\sum_{j=0}^{N} \mu(z)\, A_j\, T_j = \sum_{j=0}^{N}\sum_{r=0}^{R} a_r z^{2r}\, A_j\, T_j$$

$$= \sum_{j=0}^{N}\sum_{r=0}^{R} a_r \sum_{p=0}^{N} M_{jp}^{2r}\, A_p\, T_j , \tag{2.10}$$

where A_j is a set of coefficients and where the M_{jp}^{2r} operator is defined by equations (A.3), (A.5). Similarly, for the case of μ', we write

$$\sum_{j=0}^{N} \mu'\, A_j\, T_j = \sum_{j=0}^{N}\sum_{r=1}^{R} 2a_r r \sum_{p=0}^{N} M_{jp}^{2r-1}\, A_p\, T_j \tag{2.11}$$

We also need to express $\dot{T}_j$ and T_j'' in terms of T_j. Using the definitions (A.7) and (A.10) for D_{jp}^{1} and

D^2_{jp}, we write

$$A_j T'_j = \sum_{p=0}^{N} D^1_{jp} A_p T_j$$

$$A_j T''_j = \sum_{p=0}^{N} D^2_{jp} A_p T_j \ . \qquad (2.12a,b)$$

We substitute (2.9 - 2.12) into (2.8), and after rearranging terms, we obtain a first order equation for the coefficients V_{jk}:

$$\dot{V}_{jk} = G_{jk} \ , \qquad (2.13a)$$

where G_{jk} acts as a forcing function, given by

$$G_{jk} = \sum_{r=1}^{R} 2a_r r \sum_{p=0}^{N} M^{2r-1}_{jp} \sum_{q=0}^{N} D^1_{pq} V_{qk}$$

$$+ \sum_{r=0}^{R} a_r \sum_{p=0}^{N} M_{jp} \sum_{q=0}^{N} D^2_{pq} V_{qk}$$

$$+ (f/k\pi) \sum_{q=0}^{N} D^1_{jq} W_{qk} \ . \qquad (2.13b)$$

At this point we apply two boundary conditions. The first boundary condition,

$$\partial_z v = 0 \text{ at } z = 0 \ , \qquad (2.14)$$

is automatically satisfied by requiring

$$V_{jk} = 0 \text{ for odd } j \ . \qquad (2.15)$$

Thus, v becomes an even function in z. The second boundary condition is

$$\mu \partial_z v = -\tau^v(x,t) \text{ at } z = 1 . \tag{2.16}$$

We expand $\tau^v(x,t)$ as a truncated Fourier (sine) series in x:

$$\tau^v(x,t) = \sum_{k=1}^{M} \tau_k^v(t) \sin \pi x . \tag{2.17}$$

Combining (2.6), (2.16), and (2.17) gives

$$\mu(z=1) \sum_{j=0}^{N} \sum_{p=0}^{N} D^1_{jp} V_{pk} = -\tau^v_k(t) , \tag{2.18}$$

where the identity $T_j(1) = 1$ has been used.

We apply (2.18) by using the Tau method, discussed at great length by Gottlieb and Orszag (1977). We perform this method as described below. For computational purposes, we truncate the summation over j in (2.6), (2.7) at some odd integer N. We apply (2.13a) for j = 0, 2, 4,...,N - 3. Because of our requirement (2.15), (2.13a) is not evaluated for odd j. For j = N - 1, we add an additional term $B_k(t)$ to the right hand side of (2.13a). Thus, the highest order behavior of the solution is determined not by the dynamical equations, but by the boundary conditions. We rewrite (2.13a);

$$\dot{V}_{jk} = G_{jk} + B_k(t) \, \delta_{j,N-1} , \tag{2.19}$$

where $\delta_{j,N-1}$ is the Kronecker delta, which equals unity for $j = N - 1$, and equals zero otherwise. We take the time derivative of the boundary condition (2.18), and combine with (2.19) to obtain an expression for $B_k(t)$:

$$B_k(t) = - \left(\sum_{j=0}^{N} D^1_{j,N-1} \right)^{-1} \left[\dot{\tau}^y_k(t) + \sum_{j=0}^{N} \sum_{p=0}^{N} D^1_{jp} G_{pk} \right] . \qquad (2.20)$$

Equation (2.19), along with (2.13b) and (2.20) constitute a complete description of the time behavior of $V_{jk}(t)$. Equation (2.19) can be numerically integrated using any standard method. We choose to use a generalized Lax-Wendroff method, presented in Section 2.2.

We turn now to the solution of (2.4), which is similar to the solution of (2.5) but is second order in t and fourth order in z, and therefore a bit more complicated. As explained by Gottlieb and Orszag (1977), it is preferable to split (2.4) into two parts:

$$\partial_{tt}\theta + f\partial_{xzt}v - \partial_{zz}(\nu\partial_t\theta) + n^2\partial_{xx}w = 0 \qquad (2.21a)$$

$$\theta = \partial_{zz}w . \qquad (2.21b)$$

In order to avoid spurious unstable modes, we apply the boundary conditions

$$w = 0 \text{ at } z = 0, 1 \qquad (2.22)$$

to (2.21b). The other boundary conditions (2.3), after applying the continuity equation, (2.2e), become

$$u\theta_{zz}w = u\theta = 0 \text{ at } z = 0 \tag{2.23a}$$

$$u\theta_{zz}w = u\theta = \theta_x \pi x(x,t) \text{ at } z = 1 \tag{2.23b}$$

are applied to (2.21a), because they are appropriate only when u is not zero.

From the form of w in (2.7), it seems proper to choose a similar form for θ:

$$\theta = \sum_{k=1}^{M} \sum_{j=0}^{N} \theta_{jk}(t)\, T_j \cos k\pi x \ . \tag{2.24}$$

As we did for $u(z)$, we express $n(z)$ as an even function

$$n(z) = \sum_{r=0}^{R} b_r z^{2r} \ . \tag{2.25}$$

Substitution of (2.6), (2.7), (2.9), (2.24) and (2.25) into (2.21) yields

$$\ddot{\theta}_{jk} = F_{jk} \tag{2.26a}$$

$$\begin{aligned} F_{jk} = & -fk\pi \sum_{q=0}^{N} D^1_{jp}\, \dot{V}_{qk} \\ & + \sum_{r=2}^{R} 2a_r r(2r-1) \sum_{p=0}^{N} M^{2r-2}_{jp}\, \dot{\Theta}_{pk} \\ & - \sum_{r=1}^{R} 2a_r r \sum_{p=0}^{N} M^{2r-1}_{jp} \sum_{q=0}^{N} D^1_{pq}\, \dot{\Theta}_{qk} \\ & + \sum_{r=0}^{R} a_r \sum_{p=0}^{N} M^{2r}_{jp} \sum_{q=0}^{N} D^2_{pq}\, \dot{\Theta}_{qk} + (k\pi)^2 \sum_{r=0}^{R} b_r \sum_{q=0}^{N} M^{2r}_{jq}\, W_{qk} \end{aligned} \tag{2.26b}$$

Next, we apply the boundary conditions (2.23) to the determination of the Θ_{jk} coefficients. We can automatically satisfy (2.23a) by requiring that

$$\Theta_{jk} = 0 \text{ for even } j \ . \tag{2.27}$$

In order to satisfy (2.23b), we again apply the Tau method. We modify (2.26a) as follows:

$$\ddot{\Theta}_{jk} = F_{jk} + A_k(t)\, \epsilon_{j,N-2} \tag{2.28}$$

Again, we expand τ^x in terms of a truncated Fourier sine series;

$$\tau^x(x,t) = \sum_{k=1}^{M} \tau_k^x(t)\, \sin k\pi x \ . \tag{2.29}$$

We apply (2.23b) to (2.28), to obtain an expression for $A_k(t)$;

$$A_k(t) = \frac{1}{\mu(z=1)} \left[k\pi \ddot{\tau}_k^x(t) - \sum_{j=0}^{N} F_{jk} \right] \ . \tag{2.30}$$

We must also integrate (2.21b) to get the coefficients W_{jk}. We use the well known integration property of Chebyshev polynomials;

$$\int T_j(z)dz = \begin{cases} z + c & j=0 \\ \frac{1}{2} z^2 + c & j=1 \\ \frac{1}{2}\left(\frac{T_{j+1}}{j+1} - \frac{T_{j-1}}{j-1} \right) + c & j \geq 2 \ . \end{cases} \tag{2.31}$$

Combine (2.7), (2.21b), and (2.24), and integrate twice:

$$\sum_{\substack{j=1\\ \text{odd}}}^{N} W_{jk} T_j(z) = \sum_{\substack{j=1\\ \text{odd}}}^{N} \int dz' \int dz'' \, \Theta_{jk} \, T_j(z) \qquad (2.32)$$

We make use of (2.31) to get

$$\sum_{\substack{j=1\\ \text{odd}}}^{N} W_{jk} T_j(z) = \sum_{\substack{j=3\\ \text{odd}}}^{N} \frac{\Theta_{jk}}{4} \left[\frac{T_{j-2}}{(j+1)(j+2)} - \frac{2T_j}{(j^2-1)} + \frac{T_{j-2}}{(j-1)(j-2)} \right]$$

$$- \frac{\Theta_{1k}}{24} \left(3T_1 + T_3 \right) - cT_1 + c' T_0 \qquad (2.33)$$

where c and c' are constants of integration. We equate coefficients:

$$W_{jk} = \frac{\Theta_{j-2,k}}{4(j-1)j} - \frac{\Theta_{j,k}}{2(j^2-1)} + \frac{\Theta_{j+2,k}}{4(j+1)j}$$

for $3 \le \text{odd } j \le N-4$; otherwise

$$W_{N-2} = \frac{\Theta_{N-4,k}}{4(N-3)(N-2)} - \frac{\Theta_{N-2,k}}{2\left|(N-2)^2-1\right|} \qquad (2.34)$$

$$W_N = \frac{N-2}{4(N-1)N}$$

The constants of integration are determined by the boundary conditions (2.22). Since $T_j(0)$ is zero for odd j, we set c' to zero. Since $T_j(1)$ is unity for all j, we satisfy the boundary condition at z=1 by requiring that

$$\sum_{j=1}^{N} W_{jk} = 0 \qquad (2.35)$$

We do this by first using (2.34) to compute W_{jk} for odd $j = 3,\ldots,N$, and then by setting W_{1k} equal to

$$W_{1k} = - \sum_{j=3}^{N} W_{jk} \ . \tag{2.36}$$

This completes the analytic aspect of our solution.

2.3 NUMERICAL INTEGRATION IN TIME

Equations (2.19) and (2.28) are integrated numerically. We take our initial conditions to be zero for all dependent variables; the fluid starts from rest. The equations are marched forward in time simultaneously.

Equation (2.28) is second order in time. We render its solution analogous to that of (2.19) by breaking it up into two first order equations. We then have three ordinary differential equations, whose form can be symbolically represented by

$$\dot{\psi}_{jk} = g_{jk}(\psi) \ , \tag{2.37}$$

where g is an operating function. We use a third-order Lax-Wendroff scheme to integrate (2.37). This multistep scheme advances from the n to the n+1 time step as follows (we drop the j,k subscripts for clarity);

$$\begin{aligned} \psi(1) &= \psi^n + \frac{\Delta t}{3} g\left(\psi^n\right) \\ \psi(2) &= \psi^n + \frac{\Delta t}{2} g\left(\psi(1)\right) \\ \psi^{n+1} &= \psi^n + \Delta t g\left(\psi(2)\right) \ . \end{aligned} \tag{2.38}$$

The superscripts enclosed in parentheses denote intermediate solutions.

Roberts (1981) has examined the stability properties of a generalized k-order Lax-Wendroff scheme;

$$\psi^{(1)} = \psi^n + \frac{\Delta t}{k} g(\psi^n)$$

$$\psi^{(2)} = \psi^n + \frac{\Delta t}{k-1} g(\psi^{(1)})$$

$$\vdots$$

$$\psi^{n+1} = \psi^n + \Delta t g(\psi^{(k-1)}) \quad . \tag{2.39}$$

We note that for the lowest order k=1, (2.39) becomes the simple Euler method. As applied to the equation $\dot{\psi} = i\lambda\psi$ (with λ real) the scheme is unstable for k = 1, 2, 5, 6, 9, 10, ..., and stable for $\lambda\Delta t$ values up to an increasing k-dependent limit for k = 3, 4, 7, 8,....

Section 3
MODEL VALIDATIONS

In this section we compare numerically generated solutions with analytic solutions presented by Rubenstein (1981). We consider the case of an unstratified environment, with a uniform eddy viscosity μ. In Section 3.1 we examine the response to a surface stress which is suddenly switched on at time $t = 0$. In Section 3.2 we examine the response to an impulsive surface stress.

3.1 SURFACE STRESS CONSTANT IN TIME

The response to a (complex valued) surface stress $\tau = \tau^x + i\tau^y$ suddenly switched on at time $t = 0$ is

$$U(z,t) = u(z,t) + iv(z,t)$$

$$= 2\tau \int_0^t \frac{e^{-if\theta}}{\sqrt{4\pi\mu\theta}} \exp(-z^2/4\mu\theta)d\theta \ , \qquad (3.1)$$

and is known as Fredholm's solution. We must keep in mind that this solution is valid for a fluid of infinite depth, whose bottom boundary conditions are $U \to 0$ as $z \to -\infty$. The bottom boundary conditions imposed on our numerical model are $w = 0$, $u_z = v_z = 0$ at $z = 0$. In addition, the numerical model computes the flow within a channel of finite width; an imposed stress leads to a closed circulation pattern. The pressure field transmits information about the side walls and bottom instantaneously, even though the diffusion wave takes a long period of time to reach the bottom.

Figure 3.1 shows a comparison between the analytic solution for the surface current, represented by the solid curve, and the numerical solution. The numerical solution is shown in two formats. The open circles represent the surface current, and the closed circles represent the surface current minus the bottom (drift) current. At time $t = \pi/f$ (1/2 inertial period) the surface current vector solutions begin to diverge. A drift current appears, which is caused by the closed circulation pattern. A positive u-component of surface velocity is compensated by a negative return flow in the bottom portion of the channel. This return flow begins to rotate in the clockwise direction at the inertial frequency. This oscillating velocity vector superimposes upon the velocity profile in a manner which causes the surface velocity to drift. If we subtract the drift current from the surface current (closed circles in Fig. 3.1), then the numerical solutions agree exactly with the analytic solution.

This drifting behavior, though, does not show up in the shear profile. While the absolute values of velocity are strongly affected by the circulation pattern, the vertical shear is not significantly influenced. The shear, defined by $S(z) = [u^2(z) + v^2(z)]^{1/2}$ reaches a constant state after about half an inertial period. Figure 3.2 shows a comparison between the analytic shear profile (solid curves), computed by taking the z-derivative of (3.1) and integrating numerically, and the the numerical model solution (solid circles). Values are compared at times $t = f^{-1}$ and $2f^{-1}$, and the depth coordinate is stretched. The analytic solution is not evaluated at $z = 0$, as it is

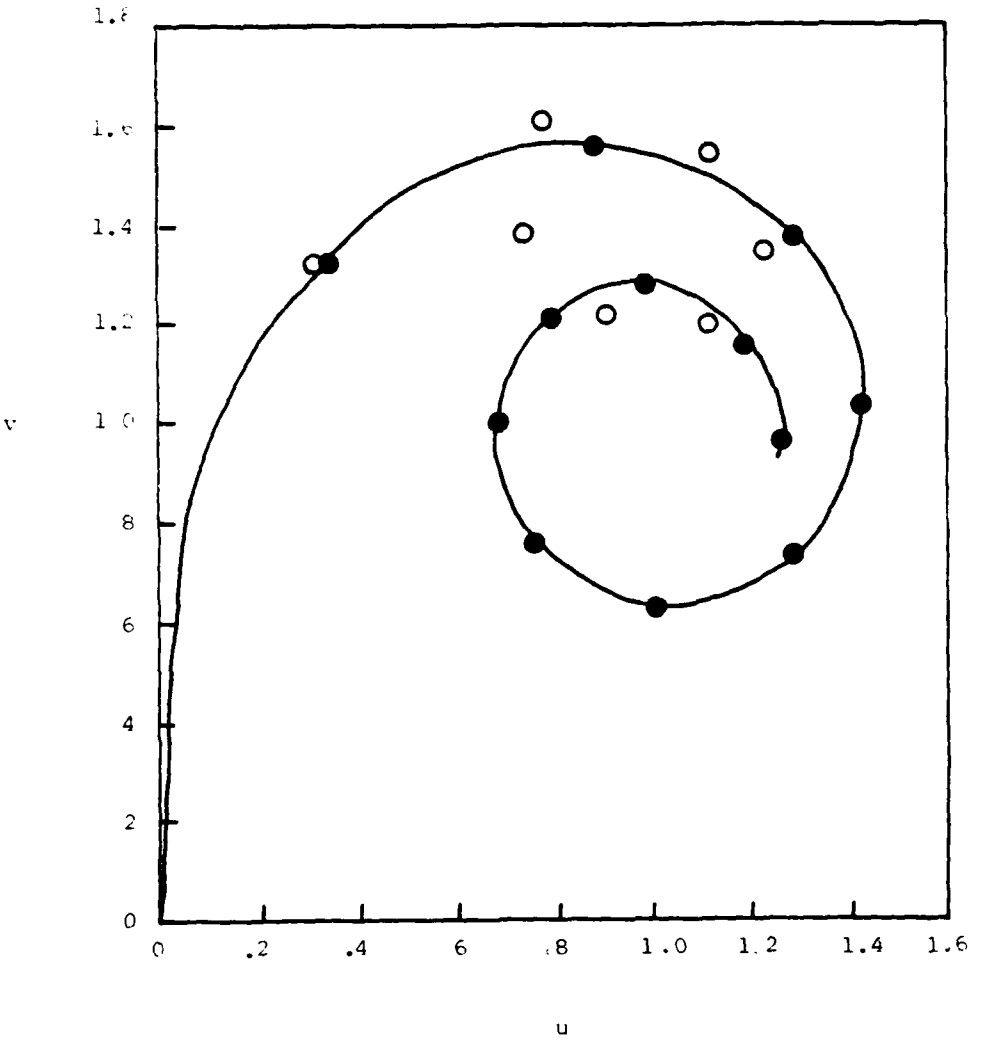

Figure 3.1 Comparison between the analytic solution (solid curve) and the numerical solution. The total surface current (open circles) begins to diverge from the analytic solution after about 1/2 inertial period. The surface current minus the bottom (drift) current, represented by closed circles, agrees exactly with the analytic solution.

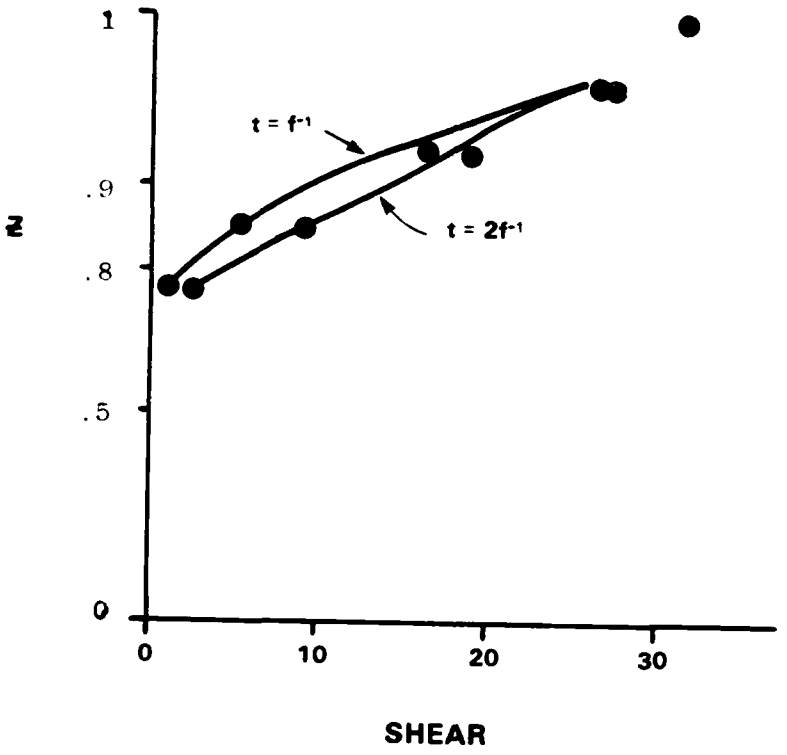

Figure 3.2 Comparison between the analytic shear profile (solid curves) and the numerical model solution (solid circles). Values are compared at times $t=f^{-1}$ and $t=2f^{-1}$. The depth coordinate is stretched.

discontinuous there. The agreement is very good, confirming our expectations that the numerical model should be well suited for computing shear.

3.2 SURFACE STRESS IMPULSE

We consider a rotational impulsive wind stress of the form

$$\tau^y = \sin\pi x \, \delta(t) \tag{3.2}$$

Rubenstein (1981) obtains an equation for the Ekman pumping velocity at depth h:

$$\ddot{w}_h + 2c\dot{w}_h + (c^2+f^2)w_h = f\hat{\underline{z}}\cdot(\nabla \times \underline{\tau}) \ . \tag{3.3}$$

Here, c is a depth-averaged drag coefficient. We can solve (3.2) - (3.3) using the method of Green's functions. If we define $\omega_o^2 = c^2 + f^2$, then the Green's function corresponding to (3.3) may be written as

$$G(t,t') = \frac{1}{\omega_o} \, e^{-c(t-t')} \sin \omega_o(t-t') \ . \tag{3.4}$$

The solution becomes

$$w_h(x,t) = -f \, \pi \cos\pi x \ \frac{e^{-ct}}{\omega_o} \sin\omega_o t \ . \tag{3.5}$$

An impulsive surface stress was applied to the numerical model, and integrated in time for about 8 inertial periods. The nondimensional vertical velocity at the nondimensional depth 0.82 is plotted in Figure 3.3 (solid curve). The dashed curve is a plot of equation (3.5), where

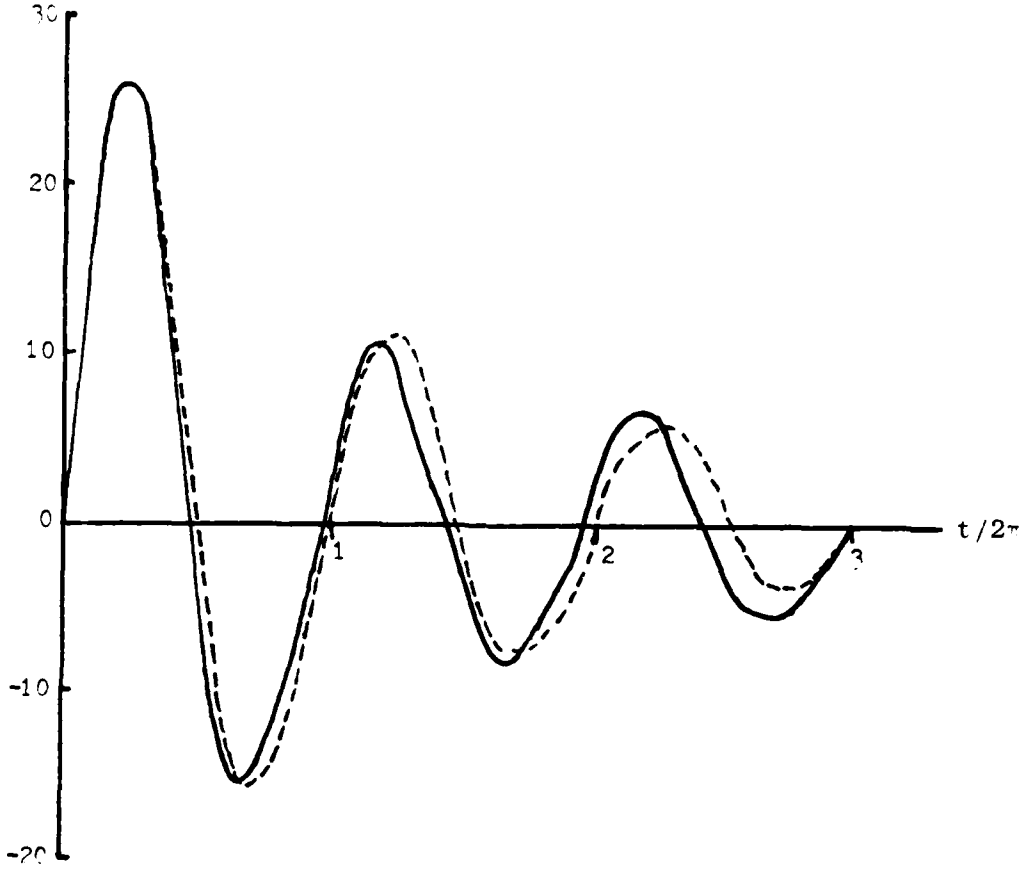

Figure 3.3 Comparison between Ekman pumping velocity computed analytically (dashed curve), and numerical solution for vertical velocity (solid curve) at nondimensional depth 0.82 (depth below surface is 18% of total depth). The total duration of the numerical run was 8 inertial periods; only the first 3 are shown here.

a multiplicative constant has been adjusted so that the curves have equal magnitudes at the first peak. We have chosen the value of c in (3.5) to be 0.13f, in order to give a reasonable fit. This value corresponds to an e-folding decay time of 1.2 inertial periods.

In order to further quantify the discrepancy in Fig. 3.3, and to illustrate the procedures used in Section 5, we present a Fourier analysis comparison of the analytic and numerical solutions. The Fourier transform $X(\omega)$ of (3.5), to within a multiplicative factor, is given by

$$X(\omega) = \int_0^\infty e^{-ct} \sin\omega_o t e^{-i\omega t}\, dt \ . \qquad (3.6)$$

The function $X(\omega)$ is complex valued; after evaluating (3.6), its magnitude may be shown to be

$$|X(\omega)| = \left\{ \frac{c^2 + \omega_o^2}{\left[c^2 + (\omega_o+\omega)^2\right]\left[c^2 + (\omega_o-\omega)^2\right]} \right\}^{1/2} \qquad (3.7)$$

Since the Fourier transform of an impulsive delta function is equal to unity, the system response function is simply the function $|X(\omega)|$ given in (3.7). Fig. 3.4 shows a comparison between the analytic response function (3.7) and the numerical solution. The solid curve represents a Fourier component estimate of the numerical model solution, and the dashed curve represents equation (3.7), modified by the same multiplicative constant mentioned above. The agreement is not quite as good for low frequencies $\omega < f$ as it is for high frequencies $\omega > f$.

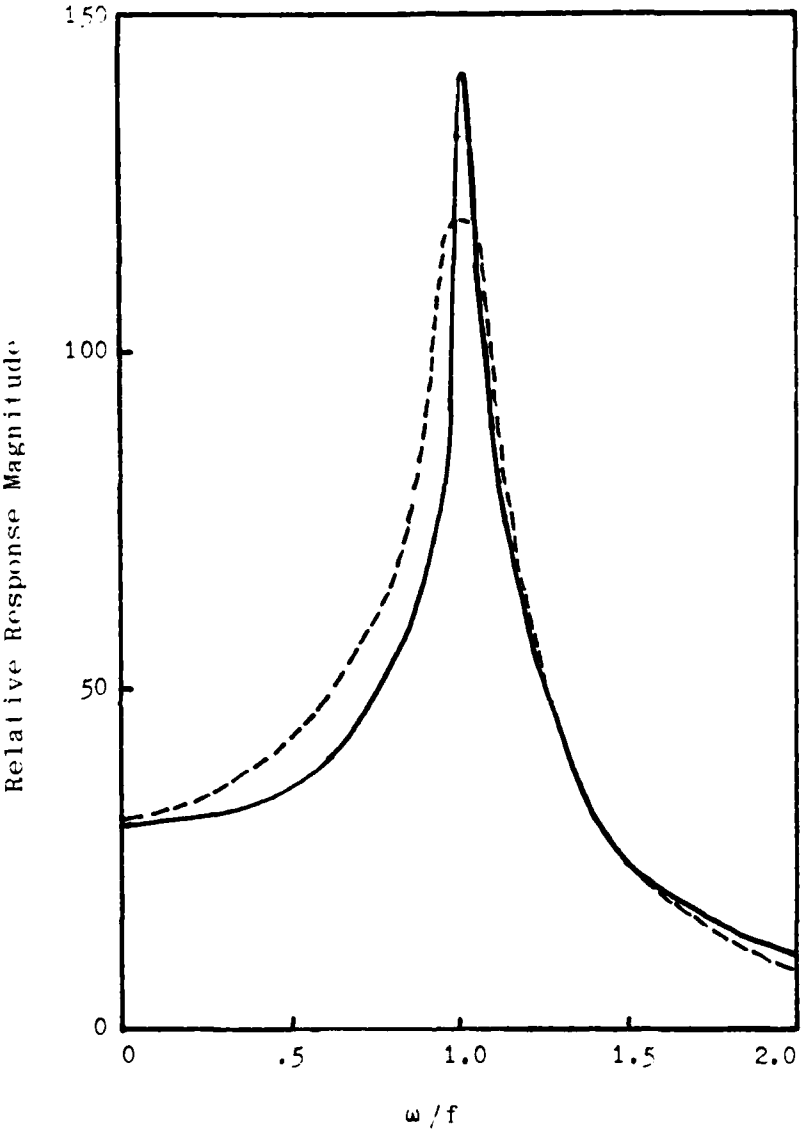

Figure 3.4 Comparison between response functions. Analytic response of Ekman pumping (dashed curve), and numerically computed vertical velocity response at nondimensional depth 0.82 (depth below surface is 18% of total depth). The total duration of the numerical simulation was 8 inertial periods.

Section 4
ANALYTIC SOLUTION TO THE INITIAL START-UP PROBLEM

4.1 NON-RESONANT SOLUTION

Before presenting our numerical results, it is a good idea to look at an analytic solution to this problem. We simplify the problem somewhat, by setting eddy viscosity to zero, and by requiring that the Vaisala frequency be uniform with depth. Then (2.4), (2.5) combine to yield the internal wave equation,

$$(\partial_{tt}+f^2)\partial_{zz}w = -n^2\partial_{xx}w \ . \qquad (4.1)$$

This equation is most appropriate in the interior, below the viscous surface layer. In effect, we have decoupled the interior from the surface layer, and we subject our system to the boundary conditions

$$w = H(t)\ \mathrm{sink}(x-Ut) \quad \text{at } z = 1, \qquad (4.2a)$$

$$w = 0 \quad \text{at } z = 0 \ . \qquad (4.2b)$$

Here, H(t) is the Heaviside step function. We define

$$g(t,k) = \frac{H(t)}{2i}\, e^{ik(x-Ut)} \ , \qquad (4.3)$$

and split (4.2a) into two parts;

$$w = g(t,k) - g(t,-k) \quad \text{at } z = 1 \ . \qquad (4.4)$$

This splitting simplifies the algebraic manipulation involved in obtaining the solution. First we solve for the response to g(t,k) given by (4.3), and then we superpose the second component solution, as indicated by (4.4).

We note that (4.1) is a separable equation. We treat (4.1) as an inhomogeneous equation, whose solution may be split into two parts:

$$w(x,z,t) = [\psi(z,t) + \phi(z,t)]e^{ikx} \ . \qquad (4.5)$$

$\psi(z,t)$ is the solution to the inhomogeneous equation with homogeneous boundary conditions, and $\phi(z,t)$ is the solution to the homogeneous equation with inhomogeneous boundary conditions. We write them in the form

$$\psi = \sum_{m=1}^{\infty} A_m(t)\sin m\pi z \ , \qquad (4.6a)$$

$$\phi = z\,\frac{H(t)}{2i}\,e^{-ikUt} \ . \qquad (4.6b)$$

Upon substitution of (4.5), (4.6) into (4.1), we get

$$\sum_{m=1}^{\infty} \left[(\partial_{tt}+f^2)m^2\pi^2 + k^2n^2 \right] A_m \sin m\pi z + k^2n^2 z\,\frac{H(t)}{2i}\,e^{-ikUt} = 0 \ . \qquad (4.7)$$

We define a set of coefficients α_m such that z may be expanded in a sine series,

$$z = \sum_{m=1}^{\infty} \alpha_m \sin m\pi z \ , \qquad (4.8a)$$

and therefore

$$\alpha_m = (-1)^{m+1} \frac{2}{m\pi} . \tag{4.8b}$$

Then (4.7) becomes

$$\left[\left(\partial_{tt} + f^2\right)\left(\frac{m\pi}{kn}\right)^2 + 1\right] A_m = -\alpha_m \frac{H(t)}{2i} e^{-ikUt} . \tag{4.9}$$

The general solution to the homogeneous equation is

$$A_m = B_m \cos\omega_m t + C_m \sin\omega_m t , \tag{4.10}$$

which leads to the dispersion relation

$$\omega_m^2 = f^2 + (kn/m\pi)^2 . \tag{4.11}$$

We use this relation to simplify (4.9):

$$(\partial_{tt}+\omega_m^2) A_m = -\alpha_m(\omega_m^2-f^2)\frac{H(t)}{2i} e^{-ikUt} , \tag{4.12}$$

and the initial conditions are

$$A_m = \dot{A}_m = 0 \text{ at } t = 0 . \tag{4.13}$$

The Green's function associated with (4.12) is

$$G(t,t') = \begin{cases} 0 & t < t' \\ \dfrac{\sin\omega_m(t-t')}{\omega_m} & t > t' . \end{cases} \tag{4.14}$$

After applying the Green's function integral, the solution is found:

$$A_m = -\frac{\alpha_m(\omega_m^2-f^2)}{4i\omega_m}\left[\frac{e^{-ikUt}-e^{-i\omega_m t}}{\omega_m+kU} + \frac{e^{-ikUt}-e^{-i\omega_m t}}{\omega_m-kU}\right] \qquad (4.15)$$

We combine the solutions (4.5), (4.6), (4.15) with the responses to both g(t,k) and g(t,-k), and obtain

$$w = -\sum_{m=1}^{\infty}\frac{\alpha_m}{2\omega_m}\left(\frac{kn}{m\pi}\right)^2\left[\frac{\sin k(x-Ut) - \sin(kx+\omega_m t)}{(\omega_m+kU)}\right.$$

$$\left. + \frac{\sin k(x-Ut) - \sin(kx-\omega_m t)}{(\omega_m-kU)}\right]\sin m\pi z \qquad (4.16)$$

$$+ zH(t)\sin k(x-Ut) .$$

The second solution component, proportional to z, is the barotropic solution, and describes the system response in the absence of stratification. The first component describes the response driven by the barotropic component.

4.2 RESONANT SOLUTION

The solution (4.16) is adequate for non-resonant conditions: $\omega_m \neq \pm kU$. As the mth mode approaches resonance, ω_m approaches kU or -kU, and one of the denominators approaches zero. In the limit where $\omega_j = kU$, the j'th modal solution is

$$w_j = \frac{\alpha_j}{2kU}\left(\frac{kn}{j\pi}\right)^2\left[-t\cos k(x-Ut)\right.$$

$$\left. + \frac{\sin(kx)\cos(kUt)}{kU}\right]\sin j\pi z. \qquad (4.17)$$

This solution shows that the amplitude of the jth mode grows linearly in time. We write this growth rate separately, for convenience:

$$\partial_t |w_j| = \frac{kn^2}{U} (j\pi)^{-3} \quad . \tag{4.18}$$

We note that the growth rate is proportional to j^{-3}.

Of course it is unlikely for any mode to remain in exact resonance for any extended period of time. However, if the driving function is very close to the resonant condition, i.e.,

$$\frac{\omega_j}{kU} - 1 \ll O(1) \quad , \tag{4.19}$$

then (4.18) is the appropriate growth rate expression for times scales of order t_o, where

$$t_o \ll (\omega_j - kU)^{-1} \quad . \tag{4.20}$$

4.3 OTHER RESONANCE CASES

4.3.1 Standing Wave Boundary Condition

It is an easy matter to compute the response to a standing wave boundary condition,

$$w(z=1) = 2H(t) \sin kx \cos\omega t \quad . \tag{4.21}$$

This boundary condition is simply equal to (4.2a), a wave propagating in the x-direction, superimposed upon a similar

wave propagating in the opposite direction, where λ has been substituted for kU. If the j'th mode is resonant, that is $\omega = \omega_j$, then from (4.17), the j'th modal solution becomes

$$w_j = \frac{\lambda_j}{\omega_j}\left(\frac{kn}{j\pi}\right)^2 \left[-t\sin(kx)\sin(\omega_j t) + \frac{\sin(kx)\cos(\omega_j t)}{\omega_j}\right] \sin j\pi z. \tag{4.22}$$

This solution is exactly analogous to (4.17), but the linearly growing term is a standing wave pattern, rather than a propagating one.

4.3.2 Impulse Boundary Condition

We can also compute the response to an impulsive (delta-function) boundary condition,

$$w(z=1) = \delta(t)\ \sin kx\ . \tag{4.23}$$

In Section 5, we use a wind stress boundary condition of this form. Its advantage lies in the fact that since its Fourier transform (in time) is unity, the temporal evolution of the solution can be simply Fourier transformed, to yield the response function of the system. In analogy to (4.17) and (4.22), the j'th modal solution is

$$w_j = \frac{-\alpha_j}{\omega_j}\left(\frac{kn}{j\pi}\right)^2 \sin kx\ \sin\omega_j t\ \sin j\pi z. \tag{4.24}$$

Section 5
MODEL RESULTS

Using our numerical model, we are able to obtain the "transfer" or "response" functions for each of the predicted physical variables, and for a variety of environmental conditions. These response functions are functions of horizontal wavenumber and frequency of the wind stress field. We choose a nondimensional wind stress vector of the form

$$\tau^x(x,t) = 0$$

$$\tau^y(x,t) = \delta(t) \sin \pi x \ . \qquad (5.1)$$

The advantage of this choice for the time dependence lies in the fact that the Fourier transform of a delta function is a constant. Therefore the response function of a given physical variable is simply its Fourier transform in the time domain.

In this section we present our results for two environmental conditions. The first condition is a uniformly stratified, uniformly diffusive environment. The second condition involves Vaisala frequency and eddy diffusivity profiles which are strongly depth dependent.

5.1 UNIFORM STR. ıFICATION AND EDDY DIFFUSIVITY

For this case we consider uniform profiles of Vaisala frequency and eddy diffusivity. For concreteness,

we let the value of eddy diffusivity be

$$\kappa^* = .005 \text{ m}^2 \text{ s}^{-1} . \qquad (?)$$

This value is chosen to be representative of typical upper ocean conditions. The asterisk indicates that the variable is dimensional.

The dimensional dispersion relation for this case is

$$\omega^2 = f^2 + \left(\frac{k^* N^*}{j\pi} D \right)^2 . \qquad (5.3)$$

Here k^* is the dimensional horizontal wavenumber, D is the basin depth, chosen to be 100 m, and j is the vertical mode number. We take the inertial frequency to be $f = 10^{-4}$ s^{-1}. In order to arrive at our equations of motion, we made the hydrostatic approximation. The dispersion relation (5.3) is only valid, then, for small k^*. For our choice D = 100 m, we restrict our use of (5.3) and of our model to values $k^* < 3$ km^{-1}.

We make a short digression here, pertaining to the scaling. All of the response functions in this section are the relative response amplitudes of the dimensional variables, u^*, w^*, etc. From (2.1), the product $k^* = \pi k/L$ times $N^* = nfL/D$ becomes

$$k^* N^* = n\pi kf/D . \qquad (5.4)$$

From the form of (5.1), the nondimensional wavenumber k was set to unity. In order to construct the response functions, the dimensionless parameter n was varied. If we wish to

consider the effect of varying N^* while holding k^* fixed, we merely vary n. If we wish to vary k^* while holding N^* fixed, we conceptually vary L, and let n vary in proportion to L^{-1}. From the form of (2.1), we see that both τ^* and u^* scale with L--therefore no additional scaling needs to be applied--the response functions of u^*, v^*, $\partial u^*/\partial z^*$, and $\partial v^*/\partial z^*$ may all be expressed as functions of k^*N^*. On the other hand, w^* does not scale with L, and the w^* response cannot be expressed as a function of k^*N^*, but only as a function of k^* or N^*, separately. We choose to show the response of w^* as a function of k^* rather than of N^*, because this projection helps us to compare the numerical results with the response computed analytically in Section 4.

In Figure 5.1 we show the response function of (dimensional) vertical velocity at a depth of 18 m below the surface. The contour labels represent the relative response amplitudes. The contours are superimposed over the dispersion relations for the lowest three vertical modes, represented by the dashed curves. We see that the velocity response is greatly emphasized in a narrow band near the first mode curve. There is also a smaller elevated response near the second mode curve. As discussed above, the response of w^* is plotted here as a function of k^*, with the value of N^* held fixed at 10^{-2} s^{-1}.

There is reasonably good agreement between the qualitative features of this response and the analytically computed response discussed in Section 4.3.2. According to equation (4.24), the resonant response to an impulsive Ekman pumping function is proportional to

$$w_j \propto \frac{\omega_j^2 - f^2}{j\omega_j} \qquad (5.5)$$

where the index j is the mode number. This proportionality indicates that along the characteristic curve (dispersion relation) of the j'th mode, the response increases with frequency. In the limit where ω_j is much greater than f, the response is almost linearly proportional to frequency. The agreement between this aspect of the proportionality relation (5.5) and the response shown in Figure 5.1 can be said to be good in a qualitative, but not in a strictly quantitative sense.

Another aspect of the proportionality relation (5.5) is that for a fixed frequency, the resonant response amplitude is inversely proportional to the mode number j. There is reasonable quantitative agreement between this aspect of the proportionality relation and the response shown in Figure 5.1.

We also note that the response is zero for $k^* = 0$. Wnen k^* is zero, the horizontal divergence $\partial u^*/\partial x^*$ is also zero. From the continuity equation (1.5), it follows that $\partial w^*/\partial z^*$ must also vanish. Since the vertical velocity at the surface (as well as at the flat bottom) is zero, the vertical velocity in the interior of the channel must be zero, too.

Figures 5.2 and 5.3 show the relative response functions for horizontal velocity (u^* component) and total shear, respectively. We note that these response contours are plotted as functions of the product k^*N^*. Again, the

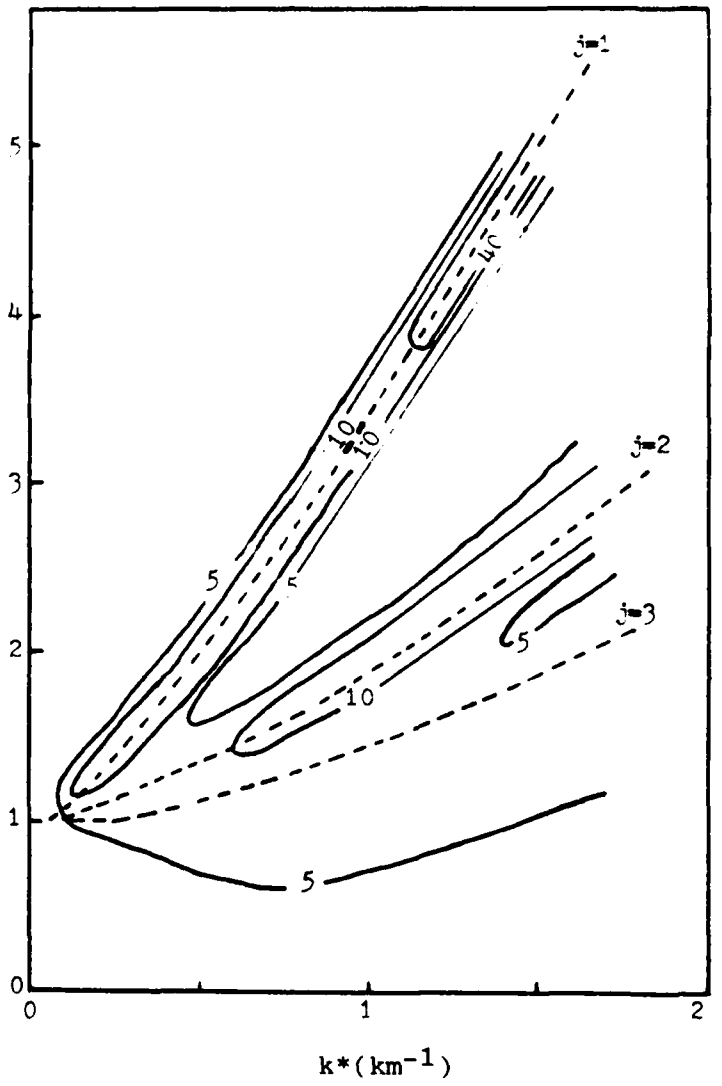

Figure 5.1 Relative amplitude response of w* velocity component, for uniform stratification and eddy diffusivity profiles. The channel depth is 100 m. This figure shows the response at a depth of 18 m below the surface (z*/D = 0.82). The dashed curves show the dispersion relations for the lowest three vertical modes.

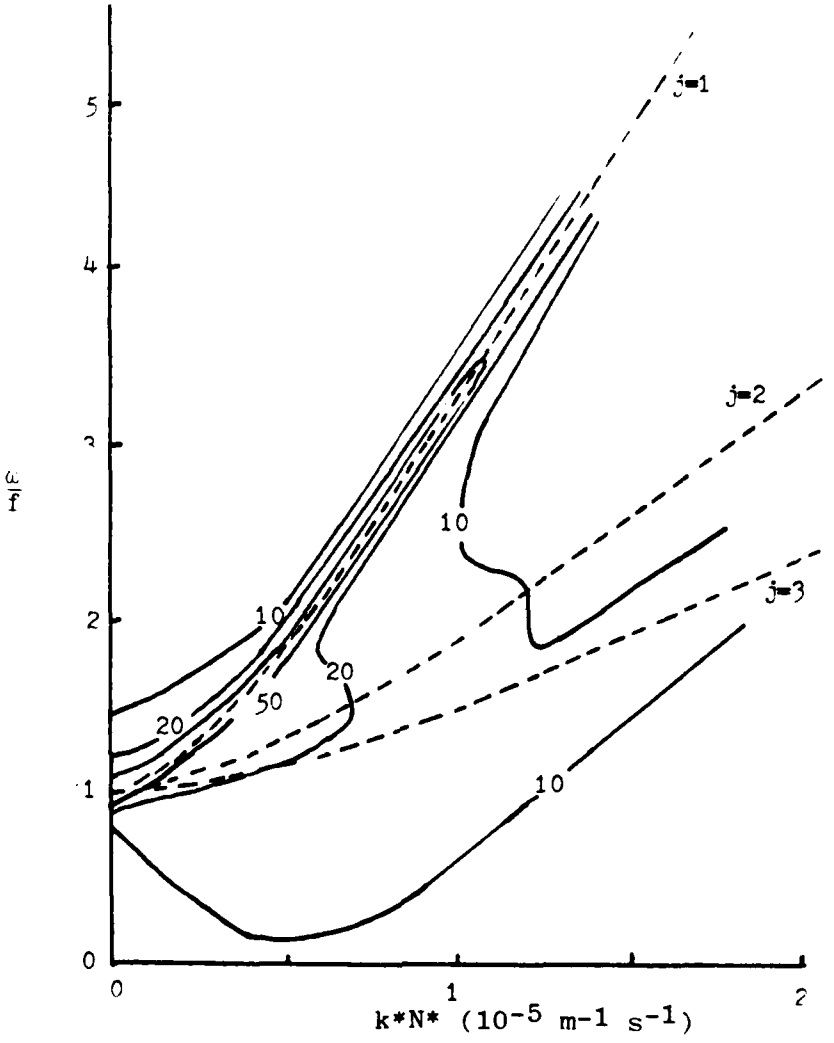

Figure 5.2 Relative amplitude response of u* velocity component, for uniform stratification and eddy diffusivity profiles. The channel depth is 100 m. This figure shows the response at a depth of 25 m below the surface (z*/D = 0.75). The dashed curves show the dispersion relations for the lowest three vertical modes.

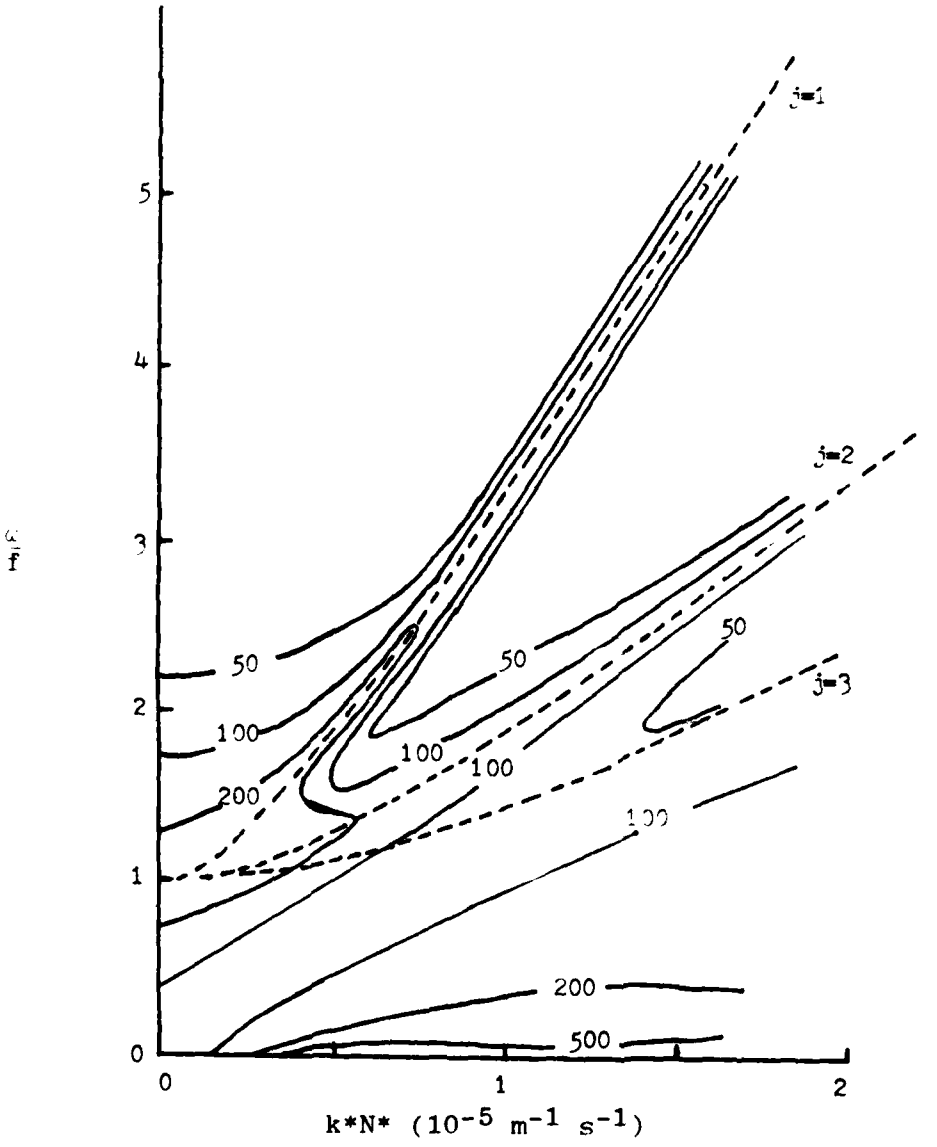

Figure 5.3 Relative amplitude response of shear for uniform stratification and eddy diffusivity profiles. The channel depth is 100 m. This figure shows the response at a depth of 25 m below the surface ($z^*/D = 0.75$). The dashed curves show the dispersion relations for the lowest three vertical modes.

response amplitudes are elevated along the dispersion relations of the lowest two modes. with the lowest mode response being the strongest. The responses of horizontal velocity and shear are different from the response of vertical velocity in two important respects. The response amplitudes of horizontal velocity and shear along characteristic curves (for the two lowest modes, $j = 1,2$) decrease with increasing frequency. Also, the response amplitudes do not vanish for $k^*N^* = 0$.

It is interesting to cast these results as functions of depth and frequency. Figures 5.4, 5.5 and 5.6 show the response amplitudes of vertical velocity, horizontal velocity, and total shear, for the special case $N^* = 0$. We note that the frequency axis, as before, is scaled by the inertial frequency f. The depth axis is scaled by the channel depth D, but is shown in stretched coordinate space, in order to show the details of the surface boundary layer.

The w^* resonance (Figure 5.4) at $\omega/f = 1$ is a very sharp function of frequency. The half-width at half-amplitude is approximately $\omega/f = 0.1$. The vertical structure at $\omega/f = 1$ is first mode, approximately of the form $w^* \propto \sin\pi z^*/D$.

The u^* resonance (Figure 5.5) is also a sharp function of frequency. The relative maxima in Figure 5.5 at $\omega/f = 1$ near the top and bottom of the channel are 180^o out of phase, since the rigid channel boundaries give rise to a closed circulation pattern. The response function for v^* was also computed, but not displayed here because it is very similar to Figure 5.5.

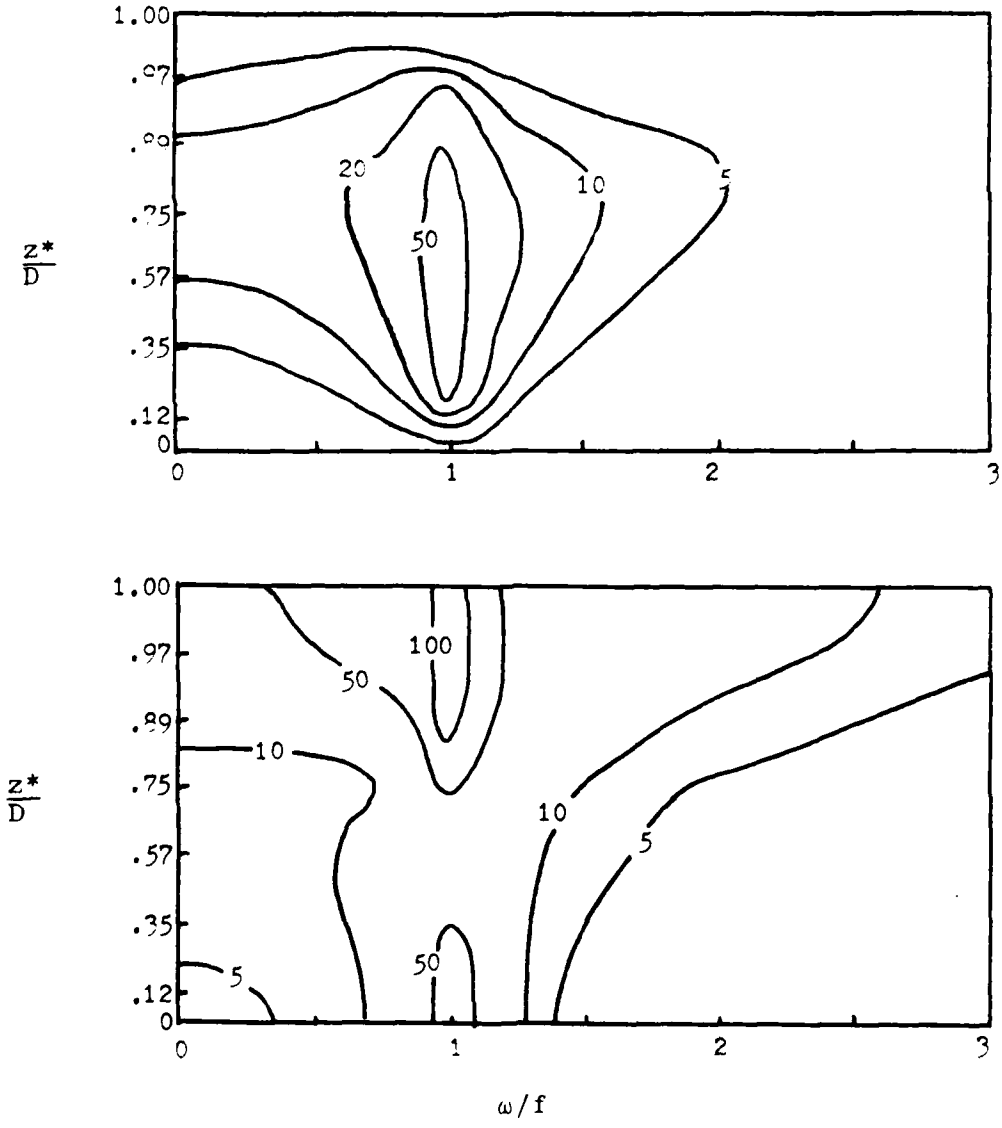

Figure 5.4 (top) Relative amplitude response of w* velocity component, for no stratification (N* = 0) and uniform eddy diffusivity profile.

Figure 5.5 (bottom) Relative amplitude response of u* velocity component, for no stratification (N* = 0) and uniform eddy diffusivity profile.

The shear response (Figure 5.6) shows a character somewhat different from that of u^* and w^*. The maximum shear occurs at the base of the surface boundary layer, at a depth of about 11 m ($z^*/D = 0.89$). In the surface boundary layer, the response is a very flat function of frequency. In the region just below the base of the boundary layer $0.89 < z^*/D < 0.75$, a transition occurs. Below this transition layer, $z^*/D < 0.75$, the shear response is a sharp resonance, centered at the inertial frequency.

We turn now to a different set of depth-frequency projections, for the case $N^* = 10^{-2}$ s^{-1}, $k^* = 0.8$ km^{-1}. Figures 5.7, 5.8, and 5.9 show the response amplitudes for w^*, u^*, and shear, respectively. In Figure 5.7 we see the vertical structure of two resonances. The first mode (j=1) resonance at $\omega/f = 2.75$ is a strong and sharp function of frequency. The second mode resonance (j=2) at $\omega/f = 1.6$ is much weaker and not nearly as sharp. The u^* response, in Figure 5.8, is analogous to the w^* response.

In Figure 5.9, the shear response has a vertical structure which is similar in character to the case for $N^* = 0$ (shown in Figure 5.6). The response is a very flat function of frequency in the surface boundary layer. In the deeper portion of the channel, $z^*/D < 0.75$, two resonances are evident. The first mode resonance is strong and sharp. The second mode resonance is somewhat weaker and flatter.

5.2 NONUNIFORM PROFILES OF STRATIFICATION AND EDDY DIFFUSIVITY

For this case we consider nonuniform profiles of stratification and eddy diffusivity. We choose a

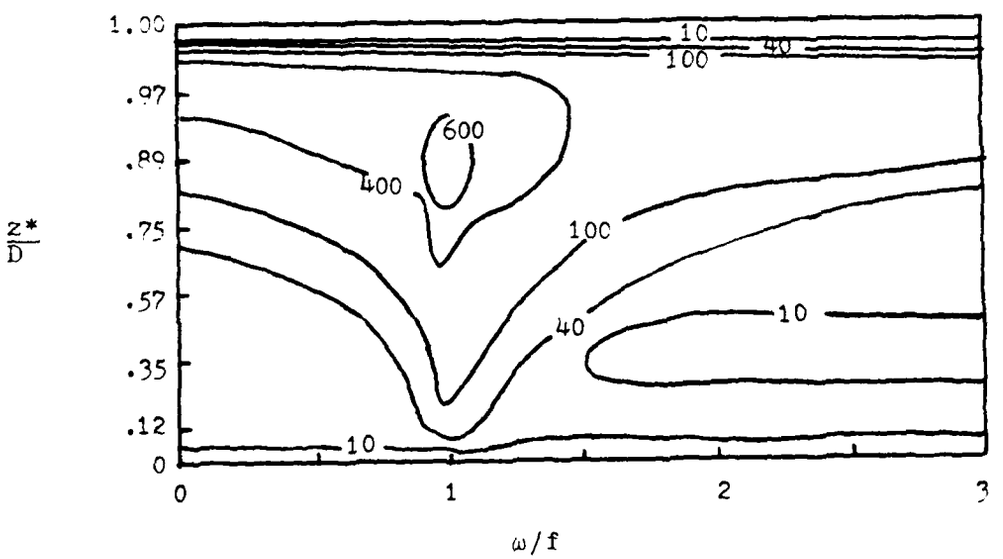

Figure 5.6 Relative amplitude response of shear, for no stratification ($N^* = 0$) and uniform eddy diffusivity profile.

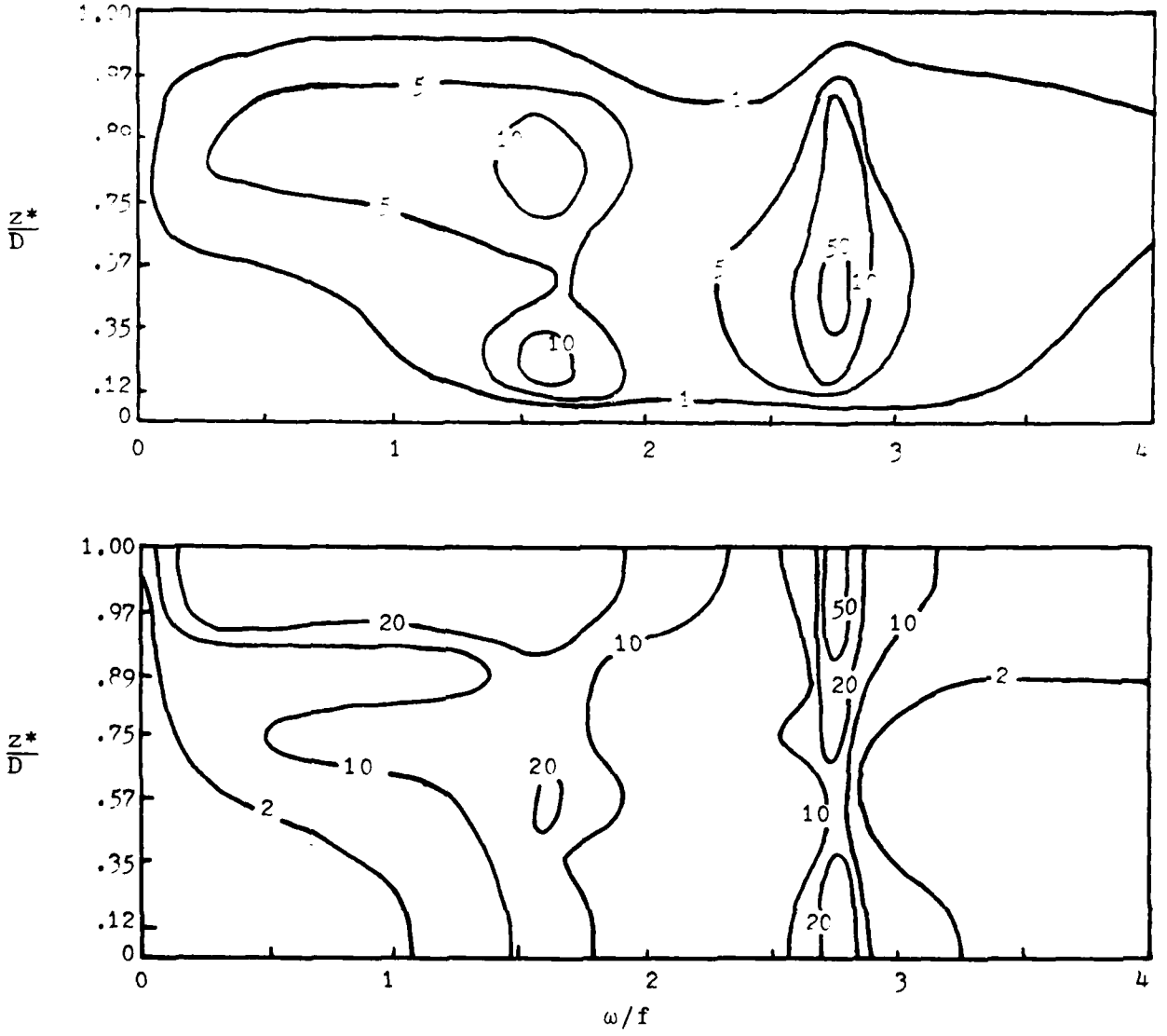

Figure 5.7 (top) Relative amplitude response of w * velocity component, for uniform stratification and eddy diffusivity profiles, as a function of depth and frequency. Horizontal wavenumber is $k^* = 0.79\ km^{-1}$.

Figure 5.8 (bottom) Relative amplitude response of u* velocity component, for uniform stratification and eddy diffusivity profiles, as a function of depth and frequency. Value of k^*N^* is $7.9 \times 10^{-6}\ m^{-1}\ s^{-1}$.

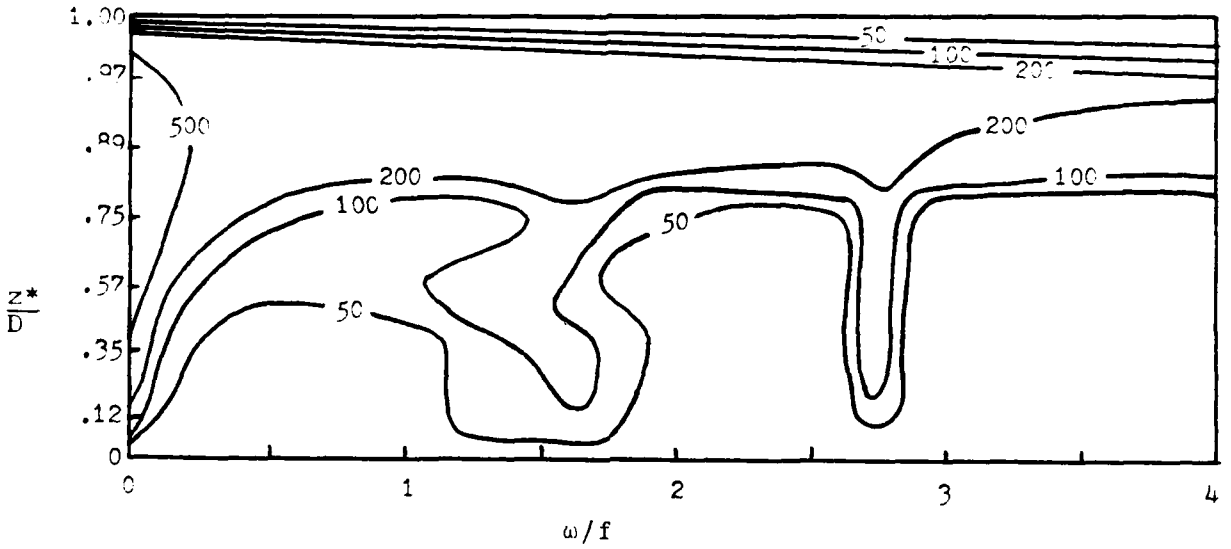

Figure 5.9 Relative amplitude response of shear, for uniform stratification and eddy diffusivity profiles, as a function of depth and frequency. Value of k*N* is 7.9×10^{-6} m^{-1} s^{-1}.

stratification profile which is modeled after one of the profiles reported by Pollard (1980) near Ocean Site D (39° 10' N, 70° W) during late July, 1970. Because the numerical model introduces an artificial bottom--in this case, at a depth of 100 m--we taper the bottom of the Vaisala frequency profile to zero. All internal wave modes should therefore reflect off their stratification profile turning points before reaching the bottom. The eddy diffusivity profile shape is patterned after that used by Krauss (e.g., 1979a). Profiles of N^{*2} and ν^* are approximated by tenth-order Chebyshev polynomials, and are displayed in Figure 5.10.

The response function for vertical velocity is shown in Figure 5.11. The first mode resonance stands out clearly, and just a mere hint of the second mode is visible. Figure 5.12 shows the response of shear. Here, too, only the first mode is readily apparent.

Figure 5.13 shows the vertical velocity response as a function of depth and frequency. The first mode resonance is strong and sharp, but the second mode resonance is much weaker. The same is true for the shear response, shown in Figure 5.14. The shear response exhibits a sharp first mode resonance in the interior. As in the case of uniform stratification and eddy diffusivity profiles, presented in Section 5.1, the shear response is a flat function of frequency in the surface boundary layer.

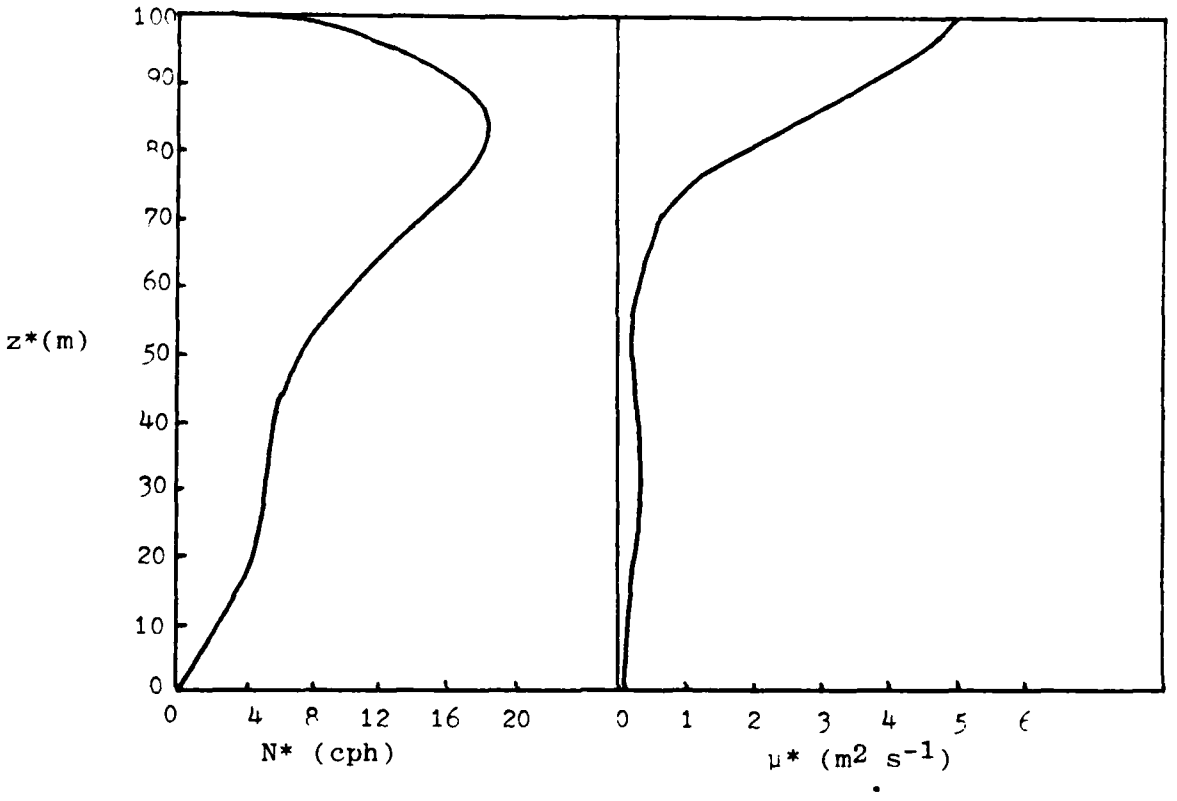

Figure 5.10 Profiles of Vaisala frequency (left) and eddy diffusivity (right) used in numerical model runs.

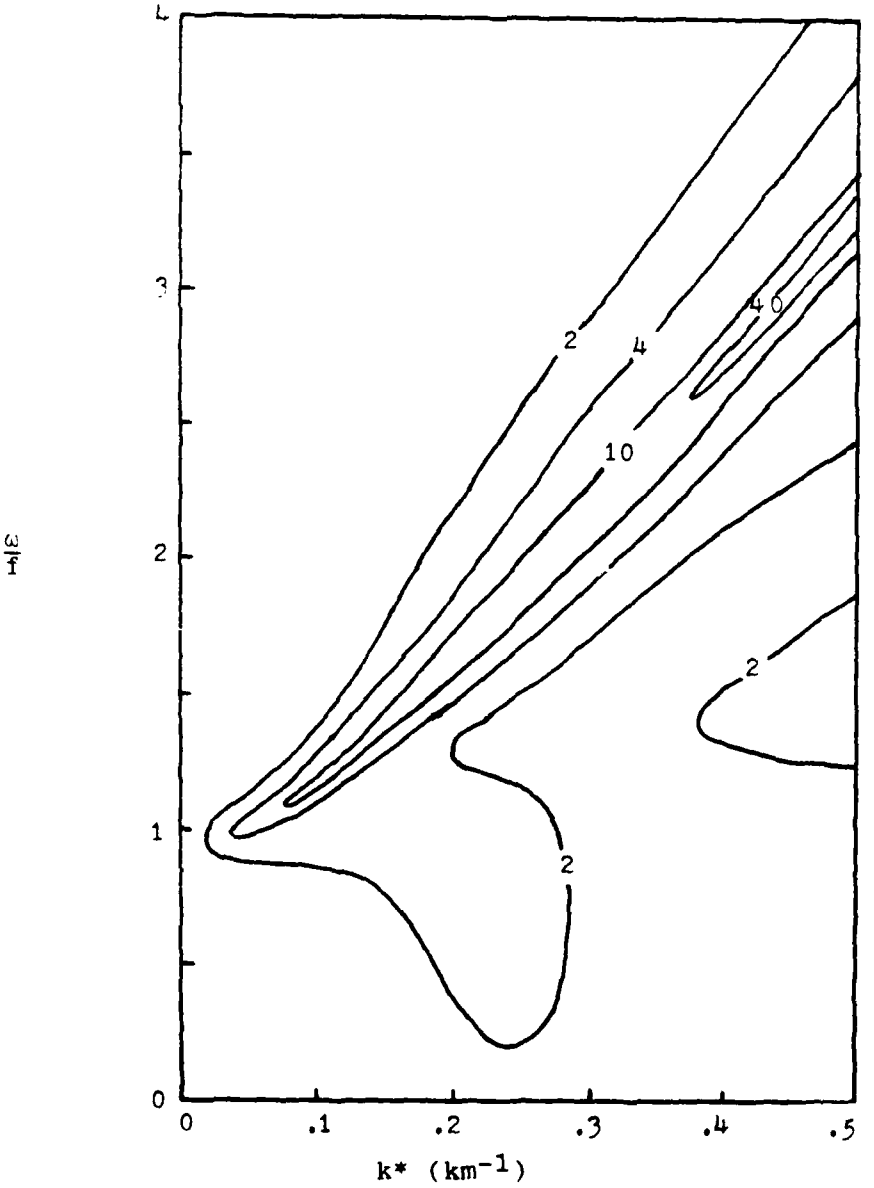

Figure 5.11 Relative amplitude response of w* velocity component, as a function of frequency and wavenumber, for the nonuniform stratification and eddy diffusivity profiles shown in Fig. 5.10. The channel depth is 100 m. This figure shows the response at a depth of 18 m below the surface (z*/D = 0.82).

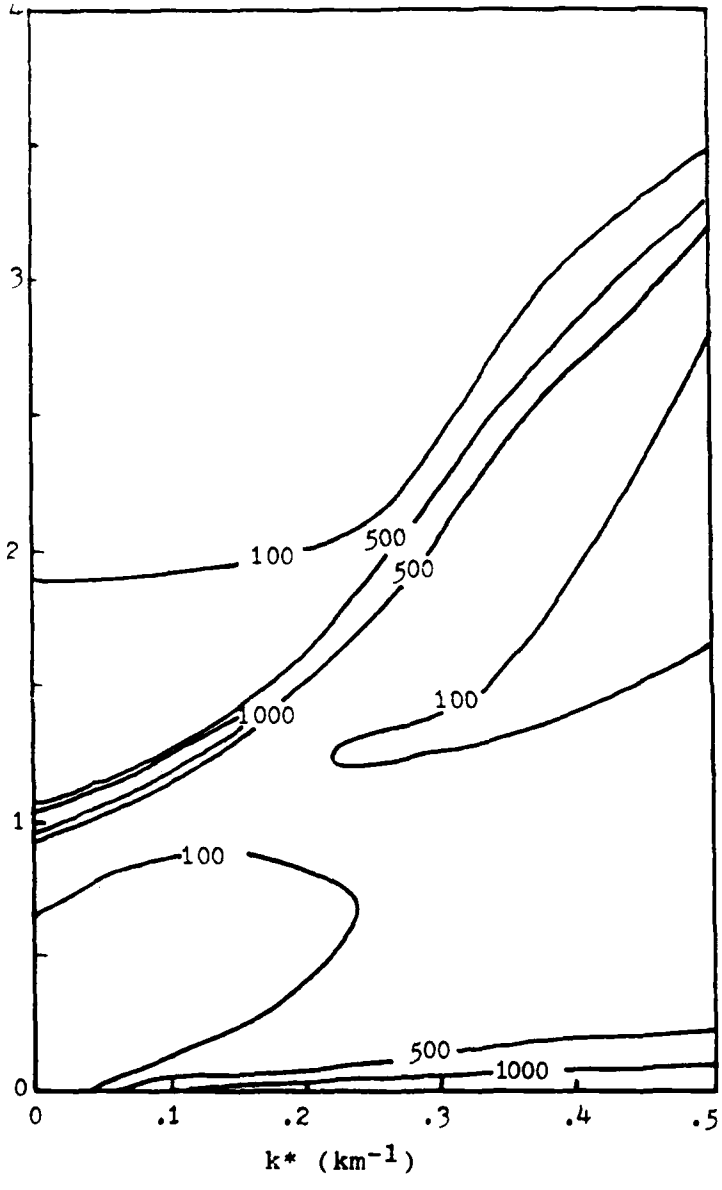

Figure 5.12 Relative amplitude response of shear, for the nonuniform stratification and eddy diffusivity profiles shown in Figure 5.10. The channel depth is 100 m. This figure shows the response at a depth of 25 m below the surface ($z^*/D = 0.75$).

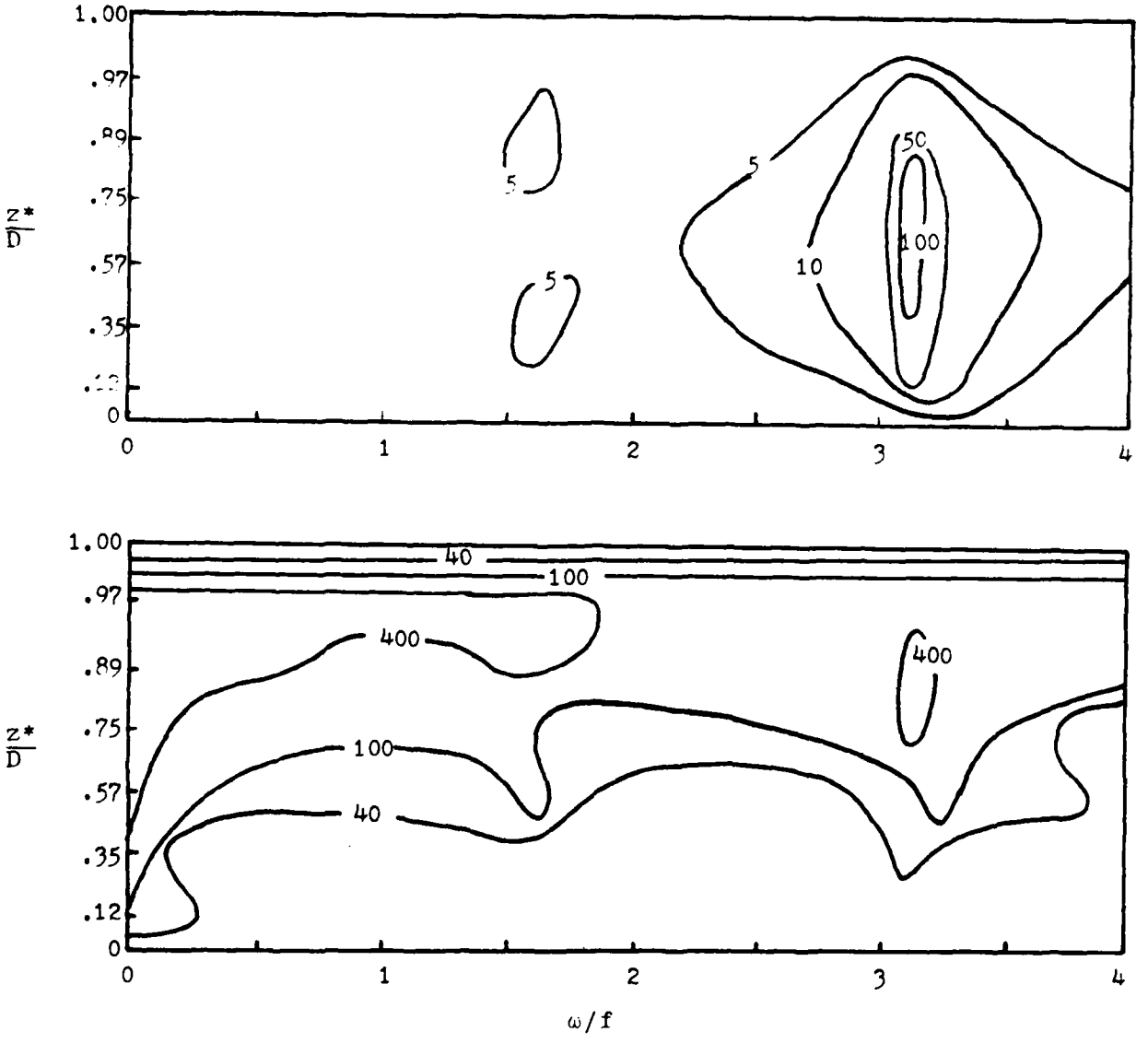

Figure 5.13 (top) Relative amplitude response of w^* velocity component, for the nonuniform stratification and eddy diffusivity profiles shown in Fig. 5.10. Horizontal wavenumber is $k^* = 0.5$ km^{-1}.

Figure 5.14 (below) As in Fig. 5.13 but for shear.

Section 6
CONCLUSIONS

In this report we present a set of dynamical equations which are suitable for describing wind-induced, near-inertial-frequency motions in the upper ocean. Krauss developed a method of solution for these equations, but we feel that his method puts constraints on the structure of the prescribed wind stress patterns which are used as input to his model. Therefore we develop a different method of solution, one that does not assume that the wind stress is periodic in time. We validate our dynamical model by presenting comparisons between numerically modeled solutions and analytic solutions. These comparisons show excellent agreement.

We present an analytical solution to the internal wave equation. We assume that the ocean may be decoupled into two components, an upper viscous surface layer, overlying a much thicker, inviscid interior layer. The surface layer is driven by a time-dependent wind stress pattern which has a sinusoidal spatial dependence. The Ekman pumping velocity at the base of the surface layer drives the interior layer. The interior solution is obtained in terms of vertical modes. Our most important result is the proportionality relation which gives the resonant amplitude of the j'th mode;

$$w_j \propto \frac{\omega_j^2 - f^2}{j\omega_j} \quad , \tag{6.1}$$

where w_j is the amplitude of the j'th mode vertical velocity, f is the inertial frequency (Coriolis parameter),

and ω_j is the eigenfrequency which satisfies the dispersion relation. For a fixed frequency, the amplitude w_j is inversely proportional to the mode number j. Along the j'th mode dispersion curve, the amplitude increases (nearly linearly) with frequency.

This result means that vertical velocity response amplitude is strongest along the dispersion relations for the lowest modes. This result is substantiated by our results from the numerical model.

The numerical results show that shear, also, is resonant at the lowest two modes. The resonances are quite strong and sharp in the channel interior. However, in the viscous surface layer--which in our specific cases extended to a depth of about 11 m--the shear response is not resonant, but is a fairly independent function of frequency. In the surface layer, fluid moves almost as a slab, and the shear deformation in this slab is nearly uniformly responsive to wind stress at all frequencies.

APPENDIX A
NOTATION FOR CHEBYSHEV EXPANSIONS

In this appendix we explain the notation used in Section 2 of the text, but we do not present derivations of properties of Chebyshev polynomials.

A.1 MONOMIAL MULTIPLYING A CHEBYSHEV EXPANSION

Consider a truncated Chebyshev polynomial expansion

$$f(z) = \sum_{j=0}^{N} A_j \, T_j(z) \tag{A.1}$$

We multiply f(z) by z, and rewrite in terms of a matrix M^1;

$$z\, f(z) = \sum_{j=0}^{N} z\, A_j \, T_j(z)$$

$$= \sum_{j=0}^{N} \sum_{p=0}^{N} M^1_{jp} \, A_p \, T_j(z) \; . \tag{A.2}$$

Here, M^1_{jp} is defined as follows;

$$M^1_{jp} = \begin{cases} 1 & \text{if } j = 1 \,,\; p = 0 \\ 1/2 & \text{if } j = p + 1 \text{ or } p = j + 1 \\ 0 & \text{otherwise .} \end{cases} \tag{A.3}$$

For a general monomial z^r multiplying f(z), we write

$$z^r f(z) = \sum_{j=0}^{N} \sum_{p=0}^{N} M^r_{jp} A_p T_j(z) , \qquad (A.4)$$

where M^r is computed from the recursion relation

$$M^r_{jp} = \sum_{q=0}^{N} M^1_{jq} M^{r-1}_{qp} \qquad (A.5)$$

A.2 DERIVATIVE OF A CHEBYSHEV POLYNOMIAL EXPANSION

We start again with (A.1), and take the first derivative, indicated by a prime, and rewrite in terms of a matrix D^1;

$$f'(z) = \sum_{j=0}^{N} A_j T'_j(z)$$

$$= \sum_{j=0}^{N} \sum_{p=0}^{N} D^1_{jp} A_p T_j(z) . \qquad (A.6)$$

Here, D^1_{jp} is defined as follows;

$$D^1_{jp} = \begin{cases} 0 & \text{if } j \geq p \text{ or } j + p \text{ is even} \\ p & \text{otherwise, if } j = 0 \\ 2p & \text{otherwise, if } j > 0. \end{cases} \qquad (A.7)$$

As an example of D^1, the N = 4 matrix is

$$D^1 = \begin{pmatrix} 0 & 1 & 0 & 3 & 0 \\ 0 & 0 & 4 & 0 & 8 \\ 0 & 0 & 0 & 6 & 0 \\ 0 & 0 & 0 & 0 & 8 \\ 0 & 0 & 0 & 0 & 0 \end{pmatrix} . \qquad \text{(A.8)}$$

The general order derivative of f(z) may be written

$$f^{(r)}(z) = \sum_{j=0}^{N} \sum_{p=0}^{N} D^r_{jp} \, A_p \, T_j(z) \, , \qquad \text{(A.9)}$$

where D^r is computed from the recursion relation

$$D^r_{jp} = \sum_{q=0}^{N} D^1_{jq} \, D^r_{qp} \, . \qquad \text{(A.10)}$$

REFERENCES

GOTTLIEB, D. and S. A. Orszag, 1977: Numerical Analysis of Spectral Methods, Cambridge Hydrodynamics, Inc., pp. 273.

ORSZAG, S. A., 1971: Accurate Solution of the Orr - Sommerfeld Stability Equation. J. Fluid Mech., 50, 689-703.

KRAUSS, W., 1976a. On currents, internal and inertial waves in a stratified ocean due to variable winds, Part 1. Deutsche Hydro. Zeitsch., 29, 87-96.

KRAUSS, W., 1976b: On currents, internal and inertial waves in a stratified ocean due to variable winds, Part 2. Deutsch Hydro. Zeitsch., 29, 119-135.

KRAUSS, W., 1978a: The response of a stratified viscous sea to moving meteorological fronts and squall lines. Deutsche Hydro. Zeitsch., 31, 16-30.

KRAUSS, W., 1978b: On the energy of the wind stress required to produce internal and inertial waves. Deutsche Hydro. Zeitsch., 31, 31-49.

KRAUSS, W., 1981: The erosion of a thermocline, J. Phys. Oceanogr., 11, 415-433.

POLLARD, R. T., 1980: Properties of near-surface inertial oscillations. J. Phys. Oceanogr., 10, 385-398.

ROBERTS, G. O. 1981: Private communication.

RUBENSTEIN, D. M., 1981: Models of Near Inertial Vertical Shear, Science Applications, Inc., Ocean Physics Division, McLean, VA. SAI-82-546-WA.

RUBENSTEIN, D. M., and F. C. Newman, 1981: Analysis of Shear from Ocean Current Meters: Progress Report I. Science Applications, Inc., Ocean Physics Division, McLean, VA. SAI-82-498-WA.

END

DATE
FILMED
1-82

DTIC